

Lattice Dynamics of Altermagnetic Ruthenium Oxide RuO_2

S. BASAK* AND A. PTOK

Institute of Nuclear Physics, Polish Academy of Sciences, W.E. Radzikowskiego 152, PL-31342 Kraków, Poland

Doi: [10.12693/APhysPolA.145.93](https://doi.org/10.12693/APhysPolA.145.93)

*e-mail: surajit.basak@ifj.edu.pl

Altermagnetic ruthenium oxide RuO_2 crystallizes with $P4_2/mnm$ symmetry. Here, we discuss the lattice dynamics of this structure. We show and discuss the phonon dispersion and density of states. The phonon dispersion curves contain several Dirac nodal lines and highly degenerate Dirac points. We present the characteristic frequencies and their irreducible representations at the Γ point. Theoretically obtained frequencies of the Raman active modes nicely reproduce the ones reported experimentally.

topics: lattice dynamics, altermagnetism, RuO_2 , DFT

1. Introduction

The altermagnetic phase is a new elementary phase of magnetically ordered systems [1, 2]. This phase is characterized by the combined features of ferromagnetic (FM) and antiferromagnetic (AFM) phases, leading to novel effects. The altermagnetic phase breaks time-reversal symmetry similar to the FM phase and possesses compensated magnetization like the AFM phase. Unlike ferromagnets, however, the altermagnetic spin splitting in the non-relativistic bands is accompanied by a symmetry-protected zero net magnetization [3]. The spin-split part of the band structure is accompanied by spin degeneracies along certain surfaces in the Brillouin zone.

Presently, several compounds realizing the altermagnetic order are known (for more details, see [4]). In our paper, we discuss the dynamical properties of RuO_2 [5], crystallized with the rutile structure (see Fig. 1). The electronic band structure exhibits spin splitting in the range of 0.5 eV [6]. Such spin band splitting should be reflected in the spin-polarized angle-resolved photoelectron spectroscopy (ARPES) measurement [7]. The time-reversal symmetry breaking [8] and the anomalous Hall effect [9] were observed experimentally. Both phenomena are related to the topological properties associated with the nonzero Berry phase [10]. Finally, a thin film of RuO_2 exhibits superconducting properties [11].

Altermagnetic RuO_2 also has several properties, interesting from an application point of view, e.g., high activation barrier [12]. This compound is a prime catalyst for the oxygen evolution reaction in water splitting [13]. In the context of thermoelectric

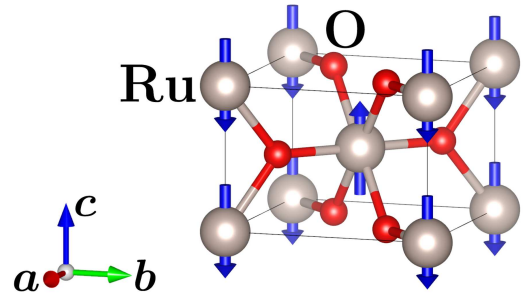


Fig. 1. The crystal structure of altermagnetic ruthenium oxide RuO_2 .

properties [14], the dynamical properties of RuO_2 can be interesting. Here, we present and discuss the dynamical properties of the altermagnetic RuO_2 .

The paper is organized as follows. The computational details are presented in Sect. 2. Next, in Sect. 3, we present and discuss our numerical results. Finally, a summary is provided in Sect. 4.

2. Computational details

The first-principles density functional theory (DFT) calculations were performed using the projector augmented-wave (PAW) potentials [15] implemented in the Vienna Ab initio Simulation Package (VASP) code [16–18]. For the exchange–correlation energy, the generalized gradient approximation (GGA) in the Perdew, Burke, and Ernzerhof (PBE) parametrization was used [19].

Similar to the previous study [7], we apply the correlation effects on Ru *d*-orbitals within the DFT+*U* approach introduced by Dudarev et al. [20]. The energy cutoff for the plane-wave expansion was set to 600 eV. Optimization of the structural parameters (in the presence of the spin-orbit coupling) was performed using a $10 \times 10 \times 15$ *k*-point grid using the Monkhorst–Pack scheme [21]. As a convergence condition of the optimization loop, we took the energy change below 10^{-6} eV and 10^{-8} eV for ionic and electronic degrees of freedom, respectively.

The dynamical properties were calculated using the direct Parlinski–Li–Kawazoe method [22] implemented in Phonopy [23]. The interatomic force constants were determined from the force acting on the atoms displaced from the equilibrium position. In these calculations, we used the supercell containing $2 \times 2 \times 3$ primitive unit cells, and reduced $4 \times 4 \times 4$ *k*-grid.

3. Results and discussion

3.1. Crystal structure

RuO₂ crystallizes with the rutile structure ($P4_2/mnm$, space group No. 136) presented in Fig. 1. It has one Ru atom sitting at each corner of a unit cell, as well as one Ru atom at the center. Each Ru atom is surrounded by six O atoms that form a distorted octahedron. In this case, the Ru and O atoms are located at Wyckoff positions 2b (0, 0, 0) and 4g ($x_O, y_O, 0$), respectively. Here, x_O and y_O are two free parameters describing the position of O atoms in the crystal structure. Theoretically, the obtained crystal parameters weakly depend on the assumed *U* [7], and in practice, *U* affects only the magnetic moment of Ru atoms. Similar to the previous study [24], we assume $U = 2$ eV for Ru *d*-orbitals. In this case, the magnetic moment of Ru is equal to $1.152 \mu_B$. After optimization, we find $a = 4.533$ Å, $c = 3.11$ Å, while the obtained free parameters are $x_O = 0.8037$ and $y_O = 0.1963$. The lattice constants are close to the experimentally observed ones, i.e., $a = 4.49$ Å, and $c = 3.11$ Å [25].

3.2. Phonon dispersion and density of states

The phonon dispersion curves are presented in Fig. 2 and are similar to the ones reported earlier [26]. The corresponding phonon density of states (DOS) is presented in Fig. 3. The vibrations in the low-frequency range (smaller than 7.5 THz) are mostly related to the Ru atoms. Similarly, higher frequency vibrations (above 14 THz) are mostly associated with vibrations of the lighter atoms, i.e., oxygen. Interestingly, vibration modes of oxygen

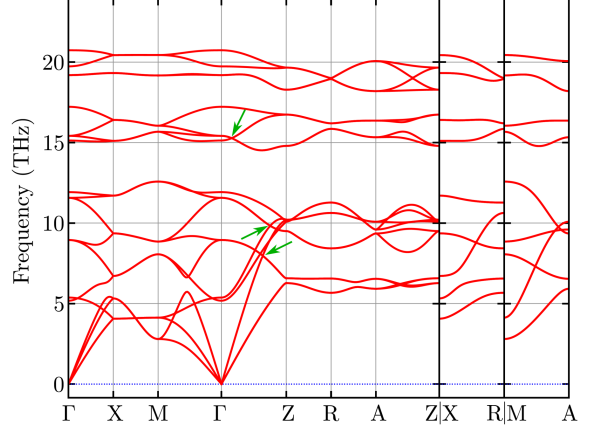


Fig. 2. The phonon dispersion curves of altermagnetic ruthenium oxide RuO₂. Green arrows mark the fourfold Dirac points along Γ -Z.

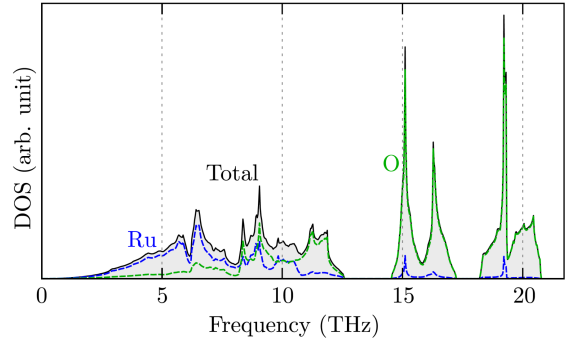


Fig. 3. The phonon density of states of altermagnetic ruthenium oxide RuO₂.

atoms at higher energies are separated from the rest of the modes by a gap. This frequency gap is well visible in the phonon band structure (Fig. 2).

In the phonon band structure, we can find several interesting features, well-known from the electronic band structure of RuO₂ [27] or non-magnetic IrO₂ with the same structure [28]. The doubly degenerate Dirac nodal lines (DNL) along the M–X path originate from the mirror symmetry along the (110) and ($\bar{1}\bar{1}0$) planes. Similarly, mirror symmetry along the (001) plane leads to double degeneracy of bands for the R–A path. Additionally, nonsymmorphic symmetry, including a fourfold screw rotation around the *z*-axis C_{4z} and a glide mirror reflection along the (100) and (010) planes, also allows the realization of doubly degenerate DNL along Γ -Z and M–A.

The degeneracy of bands along Γ -Z is the same as their degeneracy at Γ point (see also Sect. 3.3). Along M–A, all the phonon bands are doubly degenerate. Additionally, along Γ -Z, highly degenerate Dirac points can be realized, coming from the crossing of single- or doubly degenerate bands. This leads to triple and fourfold degenerate Dirac points (a few fourfold degenerate Dirac points are indicated by green arrows in Fig. 2).

3.3. IR and Raman active modes

The phonon modes at the Γ point can be decomposed into irreducible representations of the space group $P4_2/mnm$ as follows

$$\Gamma_{\text{acoustic}} = A_{2u} + E_u, \quad (1)$$

$$\Gamma_{\text{optic}} = A_{1g} + A_{2g} + A_{2u} + B_{1g} + 2B_{1u} + B_{2u} + 3E_u + E_g. \quad (2)$$

In total, there are 18 vibrational modes, eight non-degenerate ($A_{1g}, A_{2g}, 2A_{2u}, B_{1g}, B_{2g}$, and $2B_{1u}$), and ten doubly degenerate (E_g and $4E_u$). Among these, A_{2u} and E_u are infrared (IR) active, while A_{1g}, B_{1g}, B_{2g} , and E_g are Raman active. Raman active modes are related only to the oxygen atoms displacement. Contrary to this, IR active modes are related to the displacement of both Ru and O atoms.

Selection rules for Raman-active modes. The non-resonant Raman scattering intensity depends, in general, on the directions of the incident and scattered light relative to the principal axes of the crystal. It is expressed by Raman tensor R , relevant for a given crystal symmetry, as [29]

$$I \propto |\mathbf{e}_i \cdot R \cdot \mathbf{e}_s|^2, \quad (3)$$

where \mathbf{e}_i and \mathbf{e}_s are the polarization vectors of the incident and scattered light, respectively. According to group theory, the Raman tensor for the $P4_2/mnm$ space group takes the following forms for the Raman active modes

$$\begin{aligned} R(A_{1g}) &= \begin{pmatrix} a & 0 & 0 \\ 0 & a & 0 \\ 0 & 0 & b \end{pmatrix}, \\ R(B_{1g}) &= \begin{pmatrix} c & 0 & 0 \\ 0 & -c & 0 \\ 0 & 0 & 0 \end{pmatrix}, \quad R(B_{2g}) = \begin{pmatrix} 0 & d & 0 \\ d & 0 & 0 \\ 0 & 0 & 0 \end{pmatrix}, \\ R(E_g^I) &= \begin{pmatrix} 0 & 0 & 0 \\ 0 & 0 & e \\ 0 & e & 0 \end{pmatrix}, \quad R(E_g^{II}) = \begin{pmatrix} 0 & 0 & -e \\ 0 & 0 & 0 \\ -e & 0 & 0 \end{pmatrix}. \end{aligned} \quad (4)$$

Using relation (3) and the Raman tensors (4), we can determine the selection rules and Raman intensities for various scattering geometries. Table I summarizes the Raman response in the backscattering geometry for four polarization configurations. As we can see, it is possible to distinguish the Raman active modes using the different backscattering configurations. In this context, the observed Raman modes possess different insensitivity, as shown in Table I. Indeed, this technique was successfully experimentally used to recognize the Raman active modes [30, 31].

Theoretically obtained characteristic frequencies of the modes at Γ point and their irreducible representations for RuO_2 are collected in Table II. The

 TABLE I
Selection rules for Raman-active modes.

Configuration	A_{1g}	B_{1g}	B_{2g}	E_g
e_x in e_x out (linear k)	$ a ^2$	$ c ^2$	0	0
e_x in e_y out (linear \perp)	0	0	$ d ^2$	0
e_x in e_z out (linear \perp)	0	0	0	$ e ^2$

TABLE II

Symmetries of irreducible representations and their characteristic frequencies at Γ point for RuO_2 . The experimental frequencies of the Raman active modes correspond to the single-crystal measurements presented in [30].

Symm.	Freq. [THz]	Freq. [cm^{-1}]	Exp. ^a [cm^{-1}]
B_{1g}	5.180	172.79	–
B_{1u}	5.375	179.29	–
E_u	8.951	298.57	–
E_u	11.569	385.90	–
A_{2g}	11.924	397.74	–
A_{2u}	15.131	504.72	–
E_g	15.420	514.36	526
B_{1u}	17.225	574.57	–
E_u	19.193	640.22	–
A_{1g}	19.735	658.29	644
B_{2g}	20.736	691.68	714

^aFrequencies only for Raman active modes

frequencies of the Raman active modes at higher frequencies are underestimated with respect to the experimentally report ones [30]. Moreover, the ‘‘bulk’’ Raman active modes have the same frequencies as the ones reported for RuO_2 nanowires [31]. Finally, we should note that the observed frequencies can strongly depend on the experimental setup, e.g., ‘‘strain’’ [26, 30].

4. Conclusions

In this paper, we discussed the lattice dynamic of altermagnetic ruthenium oxide RuO_2 . We show that the bulk system is stable with $P4_2/mnm$ symmetry. The phonon dispersion curves are well defined, i.e., all phonon branches possess real frequencies. The vibrations at the low-frequency range are related to the Ru modes, while the branches at the high-frequency range are mostly associated with the vibration of O atoms. We also discussed the characteristic frequencies of the modes at Γ point and the selective rules of Raman active modes. The Raman active mode is distinguished within backscattering geometry measurements. Theoretically obtained frequencies of the Raman active modes nicely reproduce the experimentally reported data.

Acknowledgments

Some figures in this work were rendered using Vesta [32]. We kindly acknowledge support from the National Science Centre (NCN, Poland) under Project No. 2021/43/B/ST3/02166.

References

- [1] L. Šmejkal, J. Sinova, T. Jungwirth, *Phys. Rev. X* **12**, 031042 (2022).
- [2] L. Šmejkal, J. Sinova, T. Jungwirth, *Phys. Rev. X* **12**, 040501 (2022).
- [3] V. Gopalan, D.B. Litvin, *Nat. Mater.* **10**, 376 (2011).
- [4] Y. Guo, H. Liu, O. Janson, I.C. Fulga, J. van den Brink, J.I. Facio, *Mater. Today Phys.* **32**, 100991 (2023).
- [5] L. Šmejkal, R. González-Hernández, T. Jungwirth, J. Sinova, *Sci. Adv.* **6**, eaaz8809 (2020).
- [6] J. Zhan, J. Li, W. Shi, X.-Q. Chen, Y. Sun, *Phys. Rev. B* **107**, 224402 (2023).
- [7] A. Ptok, [arXiv:2309.02421](https://arxiv.org/abs/2309.02421), 2023.
- [8] O. Fedchenko, J. Minar, A. Akashdeep et al., [arXiv:2306.02170](https://arxiv.org/abs/2306.02170), 2023.
- [9] Z. Feng, X. Zhou, L. Šmejkal et al., *Nat. Electron.* **5**, 735 (2022).
- [10] L. Šmejkal, A.H. MacDonald, J. Sinova, S. Nakatsuji, T. Jungwirth, *Nat. Rev. Mater.* **7**, 482 (2022).
- [11] J.P. Ruf, H. Paik, N.J. Schreiber et al., *Nat. Commun.* **12**, 59 (2021).
- [12] E. Torun, C.M. Fang, G.A. de Wijs, R.A. de Groot, *J. Phys. Chem. C* **117**, 6353 (2013).
- [13] Q. Liang, A. Bieberle-Hütter, G. Brocks, *J. Phys. Chem. C* **126**, 1337 (2022).
- [14] D. Music, O. Kremer, G. Pernot, J.M. Schneider, *Appl. Phys. Lett.* **106**, 063906 (2015).
- [15] P.E. Blöchl, *Phys. Rev. B* **50**, 17953 (1994).
- [16] G. Kresse, J. Hafner, *Phys. Rev. B* **49**, 14251 (1994).
- [17] G. Kresse, J. Furthmüller, *Phys. Rev. B* **54**, 11169 (1996).
- [18] G. Kresse, D. Joubert, *Phys. Rev. B* **59**, 1758 (1999).
- [19] J.P. Perdew, K. Burke, M. Ernzerhof, *Phys. Rev. Lett.* **77**, 3865 (1996).
- [20] S.L. Dudarev, G.A. Botton, S.Y. Savrasov, C.J. Humphreys, A.P. Sutton, *Phys. Rev. B* **57**, 1505 (1998).
- [21] H.J. Monkhorst, J.D. Pack, *Phys. Rev. B* **13**, 5188 (1976).
- [22] K. Parlinski, Z.Q. Li, Y. Kawazoe, *Phys. Rev. Lett.* **78**, 4063 (1997).
- [23] A. Togo, I. Tanaka, *Scr. Mater.* **108**, 1 (2015).
- [24] K.-H. Ahn, A. Hariki, K.-W. Lee, J. Kuneš, *Phys. Rev. B* **99**, 184432 (2019).
- [25] Z.H. Zhu, J. Strempler, R.R. Rao et al., *Phys. Rev. Lett.* **122**, 017202 (2019).
- [26] M. Uchida, T. Nomoto, M. Musashi, R. Arita, M. Kawasaki, *Phys. Rev. Lett.* **125**, 147001 (2020).
- [27] V. Jovic, R.J. Koch, S.K. Panda et al., *Phys. Rev. B* **98**, 241101(R) (2018).
- [28] X. Xu, J. Jiang, W.J. Shi et al., *Phys. Rev. B* **99**, 195106 (2019).
- [29] R. Loudon, *Adv. Phys.* **50**, 813 (2001).
- [30] Y.M. Chen, A. Korotcov, H.P. Hsu, Y.S. Huang, D.S. Tsai, *New J. Phys.* **9**, 130 (2007).
- [31] M.H. Kim, J.M. Baik, S.J. Lee, H.-Y. Shin, J. Lee, S. Yoon, G.D. Stucky, M. Moskovits, A.M. Wodtke, *Appl. Phys. Lett.* **96**, 213108 (2010).
- [32] K. Momma, F. Izumi, *J. Appl. Crystallogr.* **44**, 1272 (2011).